Chapter 5
Chalcogenide Nanosheets: Optical Signatures of Many-Body Effects and Electronic Band Structure

Ivan Verzhbitskiy and Goki Eda

Abbreviations

1D	One-dimensional
2D	Two-dimensional
2P-PLE	Two-photon photoluminescence excitation
ADF	Annular dark field
ALD	Atomic layer deposition
ARPES	Angle-resolved photoemission spectroscopy
BLG	Bilayer graphene
CBM	Conduction band minimum
CDW	Charge density wave
CL	Cathodoluminescence
CVD	Chemical vapor deposition
CVT	Chemical vapor transport
DFT	Density functional theory
DoS	Density of state
dR	Differential reflectance
HOPG	Highly oriented pyrolytic graphite
jDoS	Joint density of states
MBE	Molecular beam epitaxy

I. Verzhbitskiy · G. Eda (✉)
Department of Physics, National University of Singapore,
2 Science Drive 3, Singapore 117551, Singapore
e-mail: g.eda@nus.edu.sg

G. Eda
Department of Chemistry, National University of Singapore,
3 Science Drive 3, Singapore 117543, Singapore

G. Eda
Centre for Advanced 2D Materials, National University of Singapore,
6 Science Drive 2, Singapore 117546, Singapore

T. Nakato et al. (eds.), *Inorganic Nanosheets and Nanosheet-Based Materials*,
Nanostructure Science and Technology, DOI 10.1007/978-4-431-56496-6_5

MX_2	Metal atoms (M) and chalcogen atoms (X)
IR	Infra-red
UV	Ultra-violet
PL	Photoluminescence
PLE	Photoluminescence excitation spectroscopy
SHG	Second harmonic generation spectroscopy
STEM	Scanning transmission electron microscopy
STM	Scanning tunneling microscopy
STS	Scanning tunneling spectroscopy
TA	Transient absorption
TMD	Transition metal dichalcogenide
VBM	Valence band maximum
XPS	X-ray photoelectron spectroscopy

5.1 Introduction

Layer compounds of metal chalcogenides (sulfides, selenides, and tellurides) form a large family of materials with a wide range of properties. Many transition metal and post-transition metal chalcogenides such as MoS_2 and GaS have been studied extensively since the early 60s due to their quasi-two-dimensional (quasi-2D) character and excitonic absorption properties [1–4]. Similar to graphite, many of these compounds intercalate guest molecules and ions [5], and superconductivity of such intercalation compounds has also been a subject of intense research [6, 7]. More recently, experimental observation of symmetry-protected topological surface states in bismuth selenides and tellurides have generated tremendous interest in the condensed matter physics community [8].

Metal chalcogenide layer compounds can be categorized into several groups accordingly to their chemistry. Layered transition metal dichalcogenides (TMDs) form a well-defined family consisting of about forty distinct compounds [9]. MoS_2 is an archetypal group 6 TMD well known for its naturally occurring molybdenite and its lubricating properties [10–12]. Transition metal trichalcogenides such as TiS_3 can be characterized by their unique quasi-one-dimensional (quasi-1D) structure [13]. Group 13 metal monochalcogenides such as GaS and InSe form a class of semiconducting hexagonal materials whose monolayers consist of four atomic layers [14]. Group 14 monochalcogenides are semiconductors but are found in distorted NaCl structure. Sn-based dichalcogenides are also semiconductors having the same crystal structure as some TMDs such as TiS_2 [15]. In_2Se_3 and Bi_2Se_3 share a similar crystal structure consisting of quintuple layers. Many of these compounds exhibit band gap in the visible to near-IR frequencies. Figure 5.1 shows the crystal structure (Fig. 5.1a) of different classes of layered chalcogenides and their bandgap values (Fig. 5.1b).

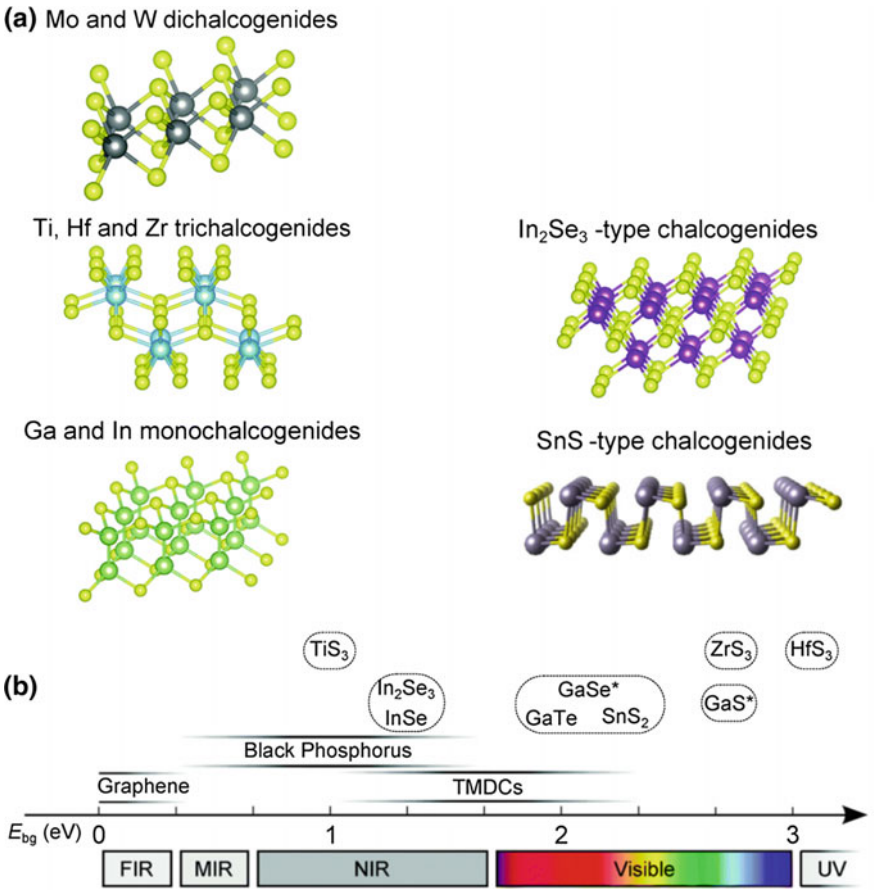

Fig. 5.1 **a** Overview of the crystal structures of layered TMDs nanosheets. The *yellow* atoms correspond to chalcogen species. **b** Bandgap of different layered semiconductors with respect to electromagnetic spectrum. The exact bandgap value would depend on the number of layers, strain level and chemical doping. Reprinted with permission from Refs. [16, 17] with slight modification (copyright 2015, Royal Society of Chemistry, American Physics Society)

While studies on chalcogenide nanosheets appear in early literatures [18], the seminal work on graphene by Geim and coworkers in 2004 [19] renewed interest in the field and led to a number of milestone studies. In particular, nanosheets of semiconducting group 6 TMDs have been extensively studied in recent years due to their emerging rich physics and potential in technological applications [20, 21]. This Chapter will introduce some basic aspects of group 6 TMDs and other semiconducting chalcogenide nanosheets with a focus on their electronic structure, excitonic properties, and spectroscopic signatures. For more general overviews, readers may be referred to recent review articles on this class of materials [22, 23].

5.2 Transition Metal Dichalcogenides

The family of TMDs shares a chemical formula of MX_2 (M: transition metal, X: chalcogen) and assumes a van der Waals layer structure in which the individual monolayer consists of a covalently bonded X–M–X sandwich. The basic properties of TMDs have been studied for over half a century (see [1] for a comprehensive review of early studies). The recent surge of interest in 2D TMDs was partly triggered by the reports on direct band gap photoluminescence (PL) from monolayer MoS_2 by two independent research teams [24, 25]. Studies further revealed a number of emerging properties inherent to mono- and few-layer sheets of MoS_2 and its isoelectronic compounds. These include optically accessible valley polarization [26, 27], large nonlinear susceptibility [28–30], piezo-electricity [31, 32], large exciton binding energy [33–35], and electrically tunable many-body states [36]. Semiconducting TMD nanosheets are effectively quantum wells but with accessible surfaces and mechanical flexibility. These unique characteristics make TMD nanosheets attractive as fundamental building blocks for novel optoelectronics and photonics applications [20–23, 37].

5.2.1 Crystal Structure

Layered TMDs occur in various polymorphs (metal coordination geometry) and polytypes (stacking order). Group 6 TMDs are stable in trigonal prismatic coordination with a 2H (2-layer unit cell, hexagonal) or a 3R (3-layer unit cell, rhombohedral) crystal structure [38]. TMDs from other transition metal groups such as TiS_2 are stable in octahedral coordination with a 1T (1-layer unit cell, trigonal) structure. For monolayer MX_2, there is no distinction between 2H and 3R polytypes. Monolayer MX_2 in trigonal prismatic coordination is non-centrosymmetric in contrast to its 2H bulk counterpart, which is centrosymmetric. This difference in crystal symmetry is responsible for some of the unique characteristics of monolayer TMDs. Some TMDs such as WTe_2 and β-$MoTe_2$ exhibit distorted 1T (1T′) crystal lattice structure [39, 40]. Polymorphism and *d*-electron count of transition metal largely determine whether TMD is metallic or semiconducting. For example, MoS_2 (formally a d^2 compound) in trigonal prismatic coordination is semiconducting whereas its octahedral polymorph is metallic (Fig. 5.2). Based on a simple ligand field model, the semiconducting nature of trigonal prismatic MoS_2 is due to the splitting between the completely filled d_{z^2} and empty d_{xy} and $d_{x^2-y^2}$ orbitals (Fig. 5.2a). In contrast, octahedral MoS_2 is metallic because of partially filled t_{2g} band (d_{xy}, d_{xz}, d_{yz}) as depicted in Fig. 5.2b. The M–X bonding states (σ) appear deep in the valence band due to its strong covalent character. The precise position of the M-X antibonding states (σ*) has been debated [1, 41] but for clarity it is shown to be above the nonbonding states in Fig. 5.2a, b.

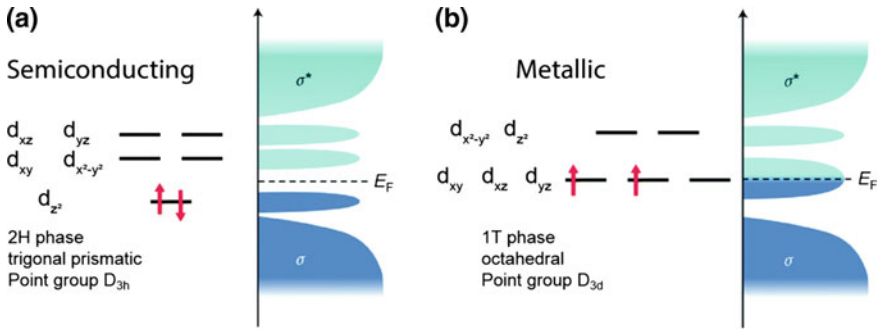

Fig. 5.2 Filling of the nonbonding *d*-orbitals for a typical d^2 TMD along with the band structure and the representative position of the Fermi level for **a** 2H phase and **b** 1T phase. Reprinted with permission from Ref. [20] with slight modification (Copyright 2013, Nature Publishing Group)

5.2.2 *Preparation*

Mono- and few-layer MX_2 can be readily obtained by micromechanical exfoliation of bulk crystals onto a substrate [42]. The starting bulk crystals can be obtained either from natural sources or synthesized by techniques such as chemical vapor transport (CVT) [43]. The size of mechanically exfoliated nanosheets is typically limited to tens of micrometers. Nanosheets can also be obtained via chemical vapor deposition (CVD), molecular beam epitaxy (MBE) [44], solution-based exfoliation techniques [45, 46], etching of bulk crystals (chemical [47, 48], plasma [49] and photothermal [50]), chemical synthesis [51], and atomic layer deposition (ALD) [52]. CVD-growth of monolayer MoS_2 [53–68], $MoSe_2$ [69, 70], WS_2 [71] and WSe_2 [72, 73] on various substrates has been demonstrated by many groups. Growth of semiconducting alloys such as MoS_xSe_{2-x} [74] and doped MX_2 [75] has also been reported. The exciton resonance features and charge transport properties of some CVD-grown monolayer samples reveal their high electronic quality equivalent to or superior to that of mechanically exfoliated counterparts.

Recent studies have shown that sulfur vacancies and antisite substitutions (S replaced by Mo) are the most commonly occurring point defects in MoS_2 [76, 77]. For bulk MoS_2, n-type doping has been attributed to donor states arising from sulfur vacancies [78]. It is believed that vacancy defects also play a role [79] in the observed strong n-type doping of monolayer MoS_2 [66, 80–82]. The reported sulfur vacancy densities vary from 3.5×10^{10} cm^{-2} in bulk MoS_2 samples [78] as measured by scanning tunneling microscopy (STM) to significantly higher values of the order of 10^{13} cm^{-2} for monolayer MoS_2 [83, 84] as measured by scanning transmission electron microscopy (STEM).

5.2.3 Energy Band Structure

Layered TMDs display a wide spectrum of electronic properties depending on the number of electrons in their nonbonding *d*-orbitals and the coordination geometry of the metal atom (see [2, 3, 85] for discussion of the crystal structure, band structure, and optical properties). As discussed above, basic electronic properties of TMDs can be predicted from filling of crystal-field-split d-orbitals. However, many interesting properties of TMD nanosheets arise from the unique dispersion of the electronic states that extend over the 2D plane. A more precise description of their electronic structure requires rigorous density functional theory (DFT) calculations. Figure 5.3a shows the electronic energy band structure of monolayer and bilayer 2H-WS_2 from DFT calculations. The key features are the two valence band hills and the two conduction band valleys. The valence band hills are at the center (Γ) and corners (K) of the Brillouin zone. On the other hand, the conduction band valleys are at the K point and the Λ point (sometimes called the Q point), which is midway between the K-Γ line. The valence band at the K point is split due to spin-orbit coupling. The conduction band also exhibits spin-orbit splitting at the K point but with a much smaller strength. In contrast to bulk WS_2, which is an indirect gap semiconductor, monolayer WS_2 is a direct gap semiconductor with the conduction band minimum (CBM) and the valence band maximum (VBM) coinciding at the K point. Bilayer WS_2 is an indirect gap semiconductor with CBM at the Λ point and the VBM at the Γ point, similar to bulk WS_2. Other group 6 TMDs such as MoS_2, $MoSe_2$, and WSe_2 exhibit similar evolution of band structure when thinned down to a single monolayer [24, 25, 86–90]. However, the indirect-to-direct crossing point is still a subject of debate for some materials such as WSe_2 [91] and $MoTe_2$ [92].

The origin of band structure evolution cannot be simply explained by quantum confinement effect. Figure 5.3a shows that the number of layers most strongly influences the conduction band valley at the Λ point (Λ_c) and the valence band hill at the Γ point (Γ_v). DFT calculations reveal that the wavefunction associated with these points consists of an admixture of the metal *d*-orbitals and the chalcogen p_z-orbitals (Fig. 5.3b). In contrast, the wavefunctions at the K_c and K_v regions exhibit predominantly *d*-character. In other words, the wavefunctions at the Λ_c and Γ_v points spatially extend to the outer surface of the X–M–X sandwich layer whereas K_c and K_v states are confined in the middle of the layer (Fig. 5.3b). Thus, the indirect band gap between the Λ_c and Γ_v points increases more rapidly with reducing number of layers compared to the direct gap at the K point, leading to a crossover in the monolayer limit.

According to a simple particle-in-a-well model, change in the band gap E_g of a 2D semiconductor should scale as $\Delta E_g = \pi^2 h^2 / 8\mu L_z^2$ where h is the Planck's constant, μ is the reduced mass of the exciton, and L_z is the thickness of the crystals [95]. This simple relation does not apply to the optical gap of TMD crystals in the few-layer thickness regime for various reasons. First, thickness reduction does not only influence carrier confinement but also average interlayer interaction,

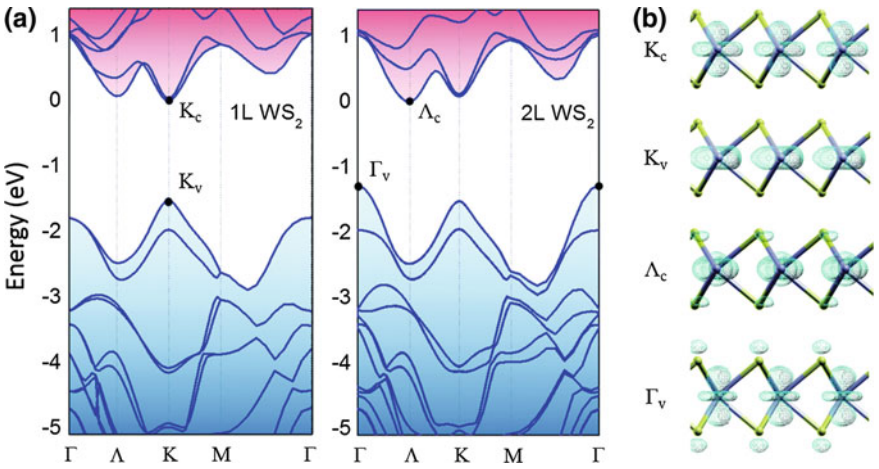

Fig. 5.3 **a** Calculated electronic band structure of mono- (*left*) and bilayer (*right*) WS_2. The *dots* indicate the valence band maximum (VBM) and the conduction band minimum (CBM). **b** Representative isosurface plot for states associated with different points of the band structure. **a** reprinted with permission from Ref. [93] with slight modification (copyright 2015, Royal Society of Chemistry), **b** reprinted with permission from Ref. [94] with slight modification (copyright 2015, American Chemical society)

thus resulting in modification of the band structure and effective mass of carriers as discussed above. Second, exciton binding energy increases rapidly with thickness reduction due to reduced screening [96]. As a result, the optical gap scales only weakly with the number of layers. Third, extrinsic effects such as unintentional doping by surface adsorbates [97] and substrate [98] obscure the band gap absorption and emission in mono- to few-layer materials.

Another important consequence of thinning group 6 TMDs down to monolayer limit is the loss of inversion symmetry and corresponding changes in the electronic structure. Since K and K′ valleys are connected by time reversal symmetry, the spin-orbit splitting is opposite in these two valleys such that they are degenerate in energy but nondegenerate in spin states. Thus, spin and valley quantum degrees of freedom are inherently coupled in monolayers. This makes the valley degrees of freedom optically accessible by circularly polarized light [99].

The hexagonal symmetry of monolayer group 6 TMDs is the same as that of monolayer graphene. The main difference is that the A and B sublattices in TMDs are occupied by metal and chalcogen atoms, respectively. The effective two-band Hamiltonian is that of a massive Dirac fermion model

$$\widehat{H} = at\left(\tau_z k_x \widehat{\sigma}_x + k_y \widehat{\sigma}_y\right) + \frac{\Delta}{2}\widehat{\sigma}_z \tag{5.1}$$

where $\tau_z = \pm 1$ is the valley index, a is the lattice constant, t is the effective nearest neighbor hopping integral, Δ is the band gap, σ is the Pauli matrices for the two

basis functions representing metal *d*-orbitals with $m = 0$ and $m = 2\tau_z$. A more complete Hamiltonian has an additional term on spin-orbit coupling, which splits the valence band top [100].

5.2.4 *Optical Signatures of Band Structure*

Linear absorption and emission spectroscopies have proven to be simple yet powerful tools to probing a number of key features of TMD nanosheets such as their electronic band structure [101], many-body interaction [102, 103], valley polarization [27], excited-state coherence [104], doping [105], defects [79], and strain [106, 107]. In 2010, Splendiani et al. [24] and Mak et al. [25] independently reported that PL from monolayer MoS_2 is distinctly stronger than that from bilayer and thicker multiplayer samples, which is contrary to the expectation that the optical response scales with the volume of the material. The authors attributed the bright PL from monolayer MoS_2 is due to its direct band gap. The emission quantum yield of indirect gap multilayer MoS_2 is substantially lower because the radiative recombination of indirect excitons is a phonon-assisted second order process and is significantly slower than non-radiative decay processes. Following these initial studies, similar observations on enhanced PL were reported for monolayer WS_2 (Fig. 5.4a), WSe_2, $MoSe_2$, and $MoTe_2$ [86, 87, 90, 92]. Figure 5.4 shows PL spectra and fluorescence image of mechanically exfoliated mono- and few-layer WS_2 sheets, demonstrating the distinctly bright PL from the monolayer region of the sample.

Absorption spectrum of group 6 TMDs exhibits characteristic excitonic resonance peaks in the near-IR to ultraviolet frequencies [1, 25]. Unlike typical

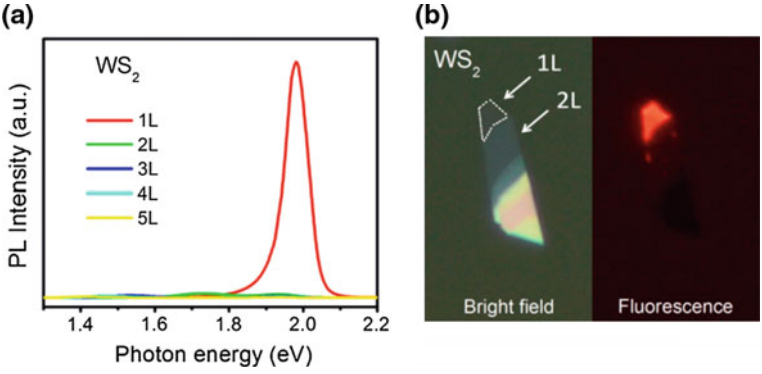

Fig. 5.4 **a** PL spectra of 1L–5L WS_2. **b** Bright field optical and fluorescence images of mechanically exfoliated WS_2. The monolayer region shows bright fluorescence compared to other multilayer regions. Adapted with permission from Ref. [86] with slight modification (Copyright 2015, American Chemical society)

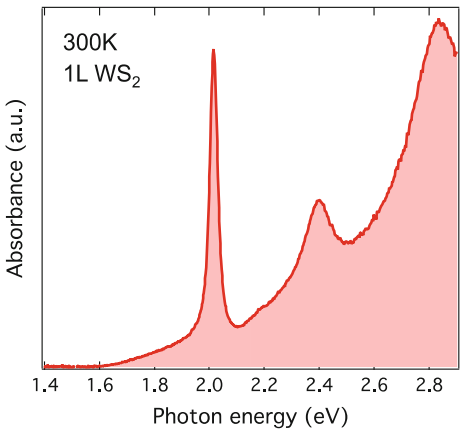

Fig. 5.5 Room temperature differential reflectance spectrum of monolayer WS_2. Note the sharp peak due to A exciton at $\sim$2 eV. Next prominent feature is due to B exciton $\sim$2.4 eV, while broad peak at $\sim$2.8 eV is due to C exciton absorption

conventional quantum wells for which free carrier absorption features dominate at room temperature, excitonic features are dominant in TMDs and obscure the onset of free carrier absorption [34, 108]. Figure 5.5 shows the room temperature absorption spectrum of monolayer WS_2 obtained by a differential reflectance measurement. A sharp ground exciton resonance feature (labeled as A) is clearly visible at $\sim$2 eV. The origin of such absorption features for bulk crystals has been discussed in early studies by Beal et al. [109] and Bromley et al. [3]. The A and B resonances are associated with excitonic transitions involving electrons in the spin-orbit-split valance band valley and the nearly degenerate conduction band valley at the K and K′ points. Thus, the energy separation of the A and B resonances roughly represent the spin-orbit interaction strength. The C absorption peak, which appears at higher energies of $\sim$2.8 eV has been attributed to band nesting, which leads to a singularity in the joint Density of States (jDoS) for 2D systems [110]. Additional peaks referred to as A′ and B′ are observed in selenides and tellurides. High quality crystals of monolayer TMDs typically absorb more than 10% of incident photons at their band gap ground exciton resonance and more strongly at the C peak resonance [111]. This unusually large absorption [112, 113] is in contrast with that of graphene, whose absorption is 2.3% in the optical frequencies [114].

Bilayer and thicker multilayer TMDs exhibit both direct and indirect exciton emission peaks. Figure 5.6a shows confinement-induced shift of PL emission peaks in 1–5 layer (L) WS_2. The shift of emission and absorption peaks are summarized in Fig. 5.6b. Indirect emission in multilayer WS_2 involves electrons and holes in the Λ and Γ valley, respectively. Thus, indirect emission peak shift indicates changes in the valley energies that are sensitive to interlayer interaction as discussed above. The direct A and B exciton energy is only weakly dependent on the number of layers while the indirect emission peak energy increases rapidly with reduction in the number of layers. It is worth noting that the hot exciton emission from B excitons is also observable at higher energies (2.3–2.4 eV).

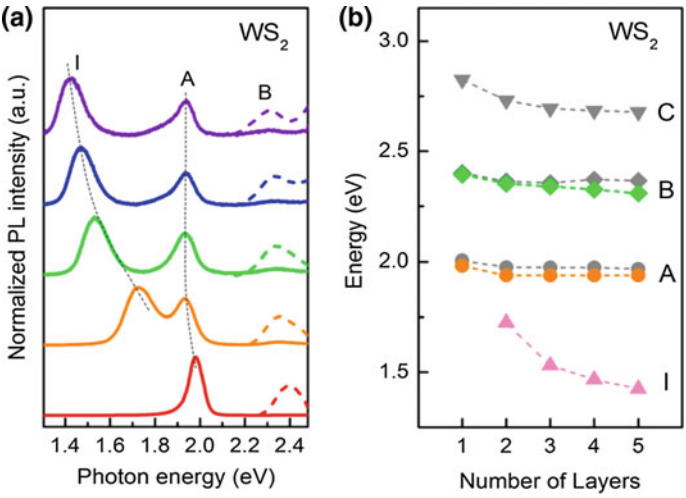

Fig. 5.6 **a** Normalized PL spectra of 1L–5L WS_2. **b** PL (*colored symbols*) and absorption (*grey symbols*) peak energies of WS_2 as a function of the number of layers. The letter *I* refers to indirect exciton peak. Reprinted with permission from Ref. [86] (Copyright 2013, American Chemical Society)

Confinement-induced shift of indirect and direct emission is a general trend reported for MoS_2, $MoSe_2$, WS_2, WSe_2, and $MoTe_2$. However, subtle details of the band structure evolution are unique to each material and are still a subject of debate. For instance, since the conduction band valleys at the K and Λ point are nearly degenerate in energy in few-layer materials, experimental determination of the CBM has been a nontrivial task. DFT results show little consensus on the conduction band structure of few-layer MX_2. For bilayer MoS_2 some calculations [96, 115] show that the CBM is located at the K point while others [24, 87, 116, 117] show that it is at the **Λ** point. On the other hand, the DFT calculations consistently show the VBM to be at the Γ point in few-layer MX_2. The calculated valence band structure shows good agreement with the experimental observations by angle-resolved photoemission spectroscopy (ARPES) [89, 118]. Direct investigation of the dispersion of unfilled conduction band states, however, is generally a challenging task. Several groups used ARPES to investigate the conduction band structure of MX_2 by introducing heavy electron doping from potassium [88]. While this approach is effective in identifying CBM, it is yet unclear how heavy doping and surface electric fields influence the band structure. Studies [119] suggest that the band renormalization effect is nonnegligible. For instance, a change in doping density by 10^{13} cm^{-2} is reported to result in a bandgap shift on the order of ~100 meV for monolayer WS_2 [120]. Large electric fields can also substantially modify the band structure according to theoretical predictions [121].

Our research team employed a less invasive approach to determining the conduction band structure in bilayer and thicker multilayer MX_2 samples [101].

In this approach, we used temperature as the knob to continuously change the band structure of the sample and studied the corresponding changes in the direct and indirect PL emission energies. Indirect emission in bilayer MX_2 involves holes in the Γ_c valley and electrons in either K_c or Λ_c valleys (Fig. 5.3). DFT calculations predict that thermal expansion of the lattice leads to opposite temperature dependence for $K_c-\Gamma_v$ gap and $\Lambda_c-\Gamma_v$ gap. We found the temperature coefficient of the indirect emission energy of bilayer WSe_2 to be negative. This suggests that the indirect optical transition involves the CBM at the K_c valley. On the other hand, the temperature coefficient for bilayer MoS_2 and WS_2 was positive, suggesting that the Λ_c valley is the CBM for these materials. Interestingly, $3 \sim 8$L WSe_2 samples showed two indirect emission peaks with opposite temperature dependence. These observations further highlight that the conduction band valleys in WSe_2 are nearly degenerate.

Ditellurides of molybdenum and tungsten exhibit multiple crystal phases that are not commonly seen in other group 6 TMDs [39, 40]. There are limited reports on the behaviors of monolayer $MoTe_2$ and WTe_2. Bulk 2H-$MoTe_2$ is an indirect gap semiconductor with a band gap of $\sim$1.0 eV. Ruppert et al. [122] reported that thinning 2H-$MoTe_2$ down to monolayer limit yields a direct gap material with an enhanced PL yield similar to the case of other group 6 TMDs. The authors concluded that multilayer samples are indirect gap semiconductors based on reduced PL emission intensities. Lezama et al. [92] further investigated low temperature absorption and emission properties of mono- and few-layer $MoTe_2$ samples and found that the PL quantum yield remains largely unchanged up to 3L sample and drops substantially for thicker materials (Fig. 5.7). These authors concluded that 2H-$MoTe_2$ remains a direct gap up to 3L, unlike MoS_2 and WS_2 that exhibit direct to indirect crossover only at the monolayer limit. Both studies agree that direct and indirect transition energies are close in energy such that indirect emission peak is not readily observable for 2H-$MoTe_2$.

It is well known that semiconducting 2H-MoS_2 and 2H-WS_2 undergo phase transformation to metallic 1T structure upon alkali metal intercalation [123, 124]. 1T phase is metastable for these materials after deintercalation and the stable 2H phase is mostly restored upon mild annealing or aging. We studied the electronic structure evolution of 1T and distorted 1T (1T′) phase of MoS_2 during progressive restoration of the stable 2H phase [125]. The samples were prepared by lithium intercalation followed by liquid phase exfoliation in water following the pioneering work by Joensen et al. [126]. X-ray photoelectron spectroscopy (XPS) analyses [127] and STEM revealed that the 2H and 1T phases coexist in the as-exfoliated materials at variable fractions. Figure 5.8a shows the optical absorption spectrum of as-produced and progressively annealed chemically exfoliated MoS_2 samples. The as-produced sample in which the metallic phase response is dominant exhibits no clear characteristic peaks of pristine 2H-MoS_2 except for the exciton-like features in the near-UV range (200–300 nm). The Drude-like broad absorption background that extends to the near-IR region below the optical gap of 2H-MoS_2 reveals the predominantly metallic character of the material. Characteristic exciton absorption and emission features of 2H-MoS_2 emerge with annealing, indicating gradual

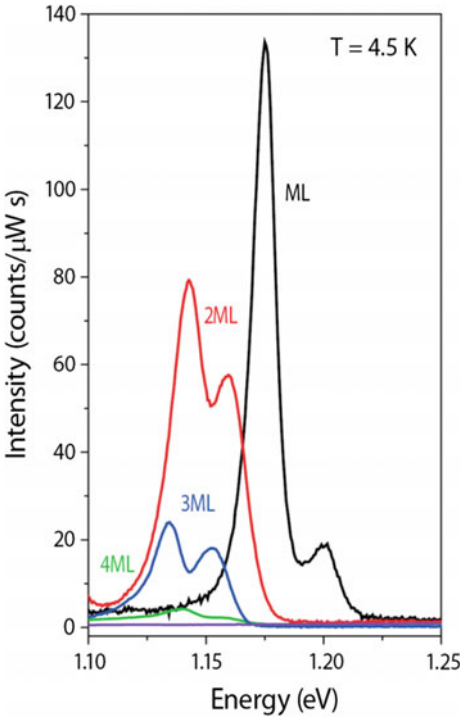

Fig. 5.7 Photoluminescence spectra of few-layer $MoTe_2$ measured at 4.5 K plotted in linear scale. Note the relative difference in intensity for 1-3L and 4L samples. Adapted from Ref. [92] (Copyright 2015, American Chemical Society)

restoration of the 2H phase. Similar to mechanically exfoliated samples, restacked nanosheets of chemically exfoliated MoS_2 exhibit thickness-dependent PL energy and intensity (Fig. 5.8b), revealing the presence of interlayer coupling despite stacking disorder.

5.2.5 *Optical Signatures of Excitons*

Layered TMDs are known as an ideal platform to study many-body effects that give rise to myriads of unique phenomena such as superconductivity [36] and charge density wave (CDW) [128]. Strong excitonic character of monolayer MX_2 is also a manifestation of enhanced many-body effects in these systems. Exciton binding energy is a measure of how strongly electrons and holes interact with each other through Coulomb forces. Its magnitude corresponds to the difference between the electronic and optical gap as schematically shown in Fig. 5.9. According to a simple hydrogen model, exciton binding energy is four times greater for 2D systems compared to bulk systems. In practice, reduced dielectric screening also enhances Coulomb interaction (Fig. 5.10). Large electron and hole effective masses in TMDs also contribute to the large exciton binding energy. The large binding

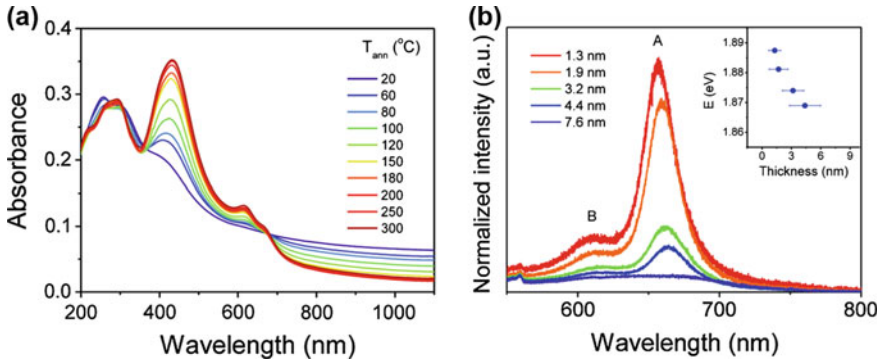

Fig. 5.8 **a** Absorption of MoS_2 thin films annealed at various temperatures. Note the restoration of A and B features (~600–700 nm) at high-temperature annealed samples. **b** PL spectra of annealed MoS_2 films as a function of film thickness. *Inset* shows peak energies extracted from PL spectra in the main panel. Note the absence of clear A exciton peak in 7.6 nm film. Reprinted with permission from Ref. [125] (Copyright 2011, American Chemical Society)

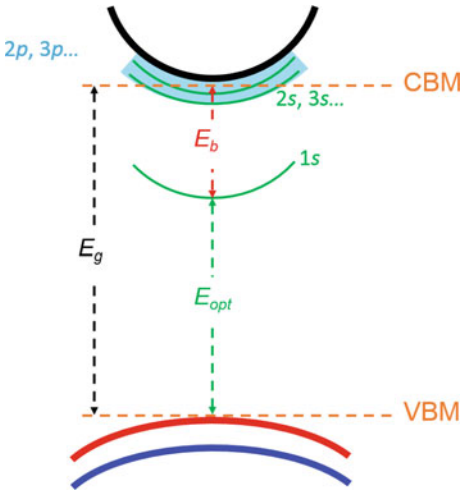

Fig. 5.9 Typical exciton excitation spectrum of monolayer group 6 TMDs. *Green lines* (1*s*, 2*s*, 3*s*, etc.) denote one-photon active states; *wide blue line* are the two-photon active states (2*p*, 3*p*, etc.). E_g, E_{opt} and E_b stands for quasiparticle gap, optical gap and binding energy, respectively

energy classifies excitons in monolayer TMDs to Frenkel-type, however, their comparatively large Bohr radius of 0.7 ~ 1 nm [108, 129] that extend over several unit cells makes them behave as Wannier-Mott excitons. Such dual-character excitons are also a fingerprint of single-wall carbon nanotubes [130].

In conventional quantum wells, the electronic gap can be identified from the onset of free carrier absorption, which has a distinct step-like function reflecting the density of states (DoS) of a 2D electronic system. As it can be seen from Fig. 5.5 excitonic absorption dominates in group 6 TMDs [108, 131] and the onset of interband transition is not immediately evident. Thus, the determination of electronic gap or conversely the exciton binding energy needs to resort to other

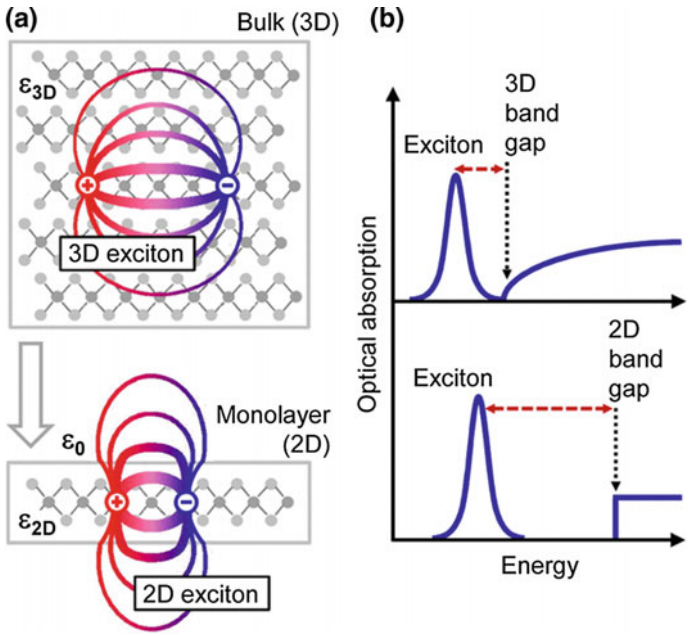

Fig. 5.10 **a** Real-space representation of bound excitons for the 3D bulk and a quasi-2D monolayer. The changes in the dielectric environment are indicated schematically by different dielectric constants ϵ_{3D} and ϵ_{2D} and by the vacuum permittivity ϵ_0. **b** Changes in the electronic and excitonic properties upon reduction of dimensionality, schematically represented by optical absorption. The transition from 3D to 2D is expected to lead to an increase of both the band gap and the exciton binding energy (indicated by the *dashed red line*). Adapted from Ref. [34] (Copyright 2014, American Physical Society)

measurement techniques. These include scanning tunneling spectroscopy (STS), ARPES, two-photon photoluminescence excitation (2P-PLE) spectroscopy, and photocurrent spectroscopy. A number of papers reporting fundamental electronic gap and exciton binding energy of various TMDs appeared in the past few years. These values are summarized in Table 5.1. While the reported values vary, exciton binding energies are typically found to be of the order of few hundreds of meV, which is one order of magnitude larger than that of conventional quasi-2D GaAs-type quantum wells [132, 133] and bulk TMDs [134].

Ugeda et al. [119] investigated the electronic gap of MBE-grown monolayer $MoSe_2$ on an epitaxial bilayer graphene (BLG) and graphite (HOPG) surface by STS. The electronic gap was measured to be 2.18 ± 0.04 eV for $MoSe_2$/BLG system. The measured optical band gap of 1.63 eV for this sample implied exciton binding energy of 0.55 eV. Further, the authors found the electronic gap of $MoSe_2$/HOPG sample to be smaller by 11% and attributed this to the different dielectric screening properties of BLG and HOPG substrates. Interestingly, the optical gap was nearly identical for the two samples, indicating that the exciton binding energy

Table 5.1 Electronic gap and exciton binding energies of quasiparticles in group 6 TMD monolayers

Material	References	E_X^0 (eV)	$E_X^{\pm}$ (eV)	E_X^2 (eV)	$E_{g,elec}$ (eV)	Substrate[a]	T (K)	Sample source[b]	Method
MoS_2	[102]		0.018				10		PL, abs
	[129]		0.032				5		abs
	[135]	0.57			2.5	susp.	77	CVD	Photocurrent
	[33]	0.22–0.42			2.15–2.35	HOPG	77	CVD	STS, PL
	[145]			0.07			74	CVD	TA[c]
	[146]			0.04, 0.06		Al_2O_3	10		TA
WS_2	[147]		0.02–0.04				4		PL
	[137]	0.71	0.034		2.73		10		PL, 2P-PLE
	[35]	0.7					10		2P-PLE
	[34]	0.32			2.41		5		dR
	[148]		0.043	0.065			4		PL
	[149]		0.01–0.015	0.045			4		PL
$MoSe_2$	[119]	0.55			2.18	BLG	77	MBE	STS, PL
	[119]	0.27			1.94	HOPG	77	MBE	STS, PL
	[150]				2.1	HOPG	4	MBE	STS, PL
	[105]		0.03				55		PL
	[91]	0.5			2.15	HOPG	79	MBE	STS
WSe_2	[104]		0.024–0.04				30		PL
	[151]	0.37			2.02		300		2P-PLE
	[152]	0.6[d]					4		SHG[f], 2P-PLE
	[103]			0.052			50		PL
	[91]	0.5			2.12[e]	HOPG	79	CVD	STS
$MoTe_2$	[92]		0.025				4.5		PL
	[153]	0.58	0.024, 0.027		1.8	gel film[g]	300		PLE

[a]SiO_x/Si substrate is used if not mentioned otherwise

[b]Flakes were exfoliated from bulk crystal if not mentioned otherwise

[c]Transient absorption (TA)

[d]The quasiparticle bandgap was calculated (GW-BSE) to be 2.73 eV [152]

[e]Quasiparticle gap in monolayer WSe_2 was found to be indirect (from Q to K). However, similarly accessed direct gap (from K to K, ~2.20 eV) was found to nearly degenerate with indirect [91]

[f]Second harmonic generation (SHG) spectroscopy

[g]Elastic (PDMS-like) GEL film by Gel-Pack was used as the substrate

was reduced by as much as 51% for the $MoSe_2$/HOPG sample. It is worth noting that the electronic gap of similarly prepared but heavily potassium-doped monolayer $MoSe_2$ on BLG was measured to be 1.58 eV by ARPES by Zhang et al. [88]. These reports indicate that band renormalization effect is significant in these materials.

Zhang et al. [33] conducted similar STS investigation on CVD-grown monolayer MoS_2 on a HOPG surface. These authors found the electronic gap and exciton binding energy to be 2.15 ± 0.06 and 0.22 eV, respectively, at 77 K. Klots et al. [135] utilized photocurrent spectroscopy to measure the electronic gap of mechanically exfoliated and suspended monolayer MoS_2. The authors attributed the step-like increase in photocurrent at ~2.5 eV to the onset of interband transition, and reported a significantly larger exciton binding energy of 0.57 eV. The discrepancies may be related to different dielectric screening effects in suspended and supported samples.

Chernikov et al. [34] proposed a simpler approach based purely on linear optical spectroscopy to estimate the exciton binding energy of monolayer WS_2 on a SiO_2/Si substrate. This requires examination of low temperature reflectance contrast (differential reflectance, dR) spectrum of a high quality sample. As shown in Fig. 5.11, derivative of reflectance contrast reveals higher lying exciton transition features that can be identified as 2*s*, 3*s*, 4*s*, and 5*s* states of the A exciton. Assuming 2D hydrogenic Rydberg series for the 3*s*, 4*s*, and 5*s* states, the authors extract an electronic gap to be 2.41 ± 0.04 eV, which yields an exciton binding energy of 320 meV. The same group [136] confirmed the assignment of higher lying exciton transitions using photoluminescence excitation spectroscopy (PLE). Interestingly,

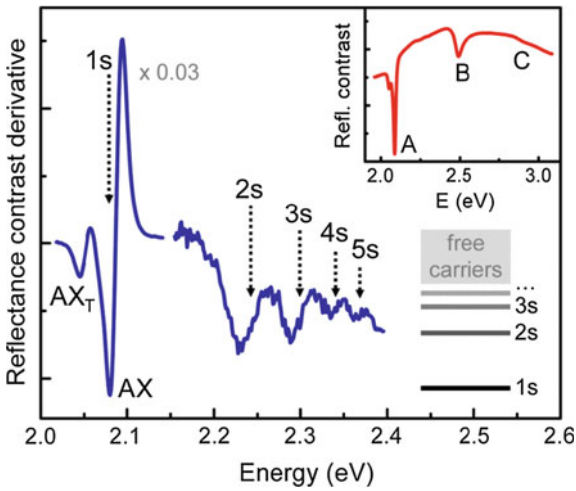

Fig. 5.11 The first derivative of the reflectance contrast spectrum of the WS_2 monolayer. The notion 1*s*, (2*s*, 3*s*,…, 5*s*) stands for exciton ground state and the higher excited states. Neutral 1*s* transition (AX) accompanied by the trion peak (AX_T) at the low-energy shoulder, this part of the spectrum is scaled for clarity. The *Inset* shows the as-measured reflectance contrast for comparison, allowing for the identification of the A, B, and C transitions. Adapted from Ref. [34] (Copyright 2014, American Physical Society)

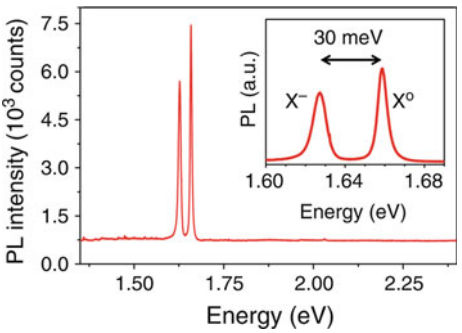

Fig. 5.12 PL spectrum of monolayer $MoSe_2$ at 20 K shows neutral exciton (X^o) and the lower energy charged exciton (trion, X^-). *Inset* shows PL of the exciton and trion peaks. Trion energy was estimated to be ~30 meV. Adapted from Ref. [105] (Copyright 2013, Nature publishing group)

this binding energy is nearly half of what was measured in the same material in nonlinear optical excitation. While *s* exciton states (1*s*, 2*s*, 3*s*,…) are accessible via one-photon excitation, *p* states (2*p*, 3*p*,…) can only be probed through two-photon spectroscopy. Ye et al. [35] and Zhu et al. [137] employed 2P-PLE spectroscopy to probe 2*p* and 3*p* states of A excitons in monolayer WS_2. These dipole-forbidden states were found at energies close to the 2*s* and 3*s* states measured by one-photon excitation.

Exciton complexes such as trions and biexcitons are also indications of strong many-body Coulomb interactions. A trion or a charged exciton is a quasi-particle consisting of either two electrons and one hole (negative trion) or two holes and one electron (positive trion) [138]. These particles have been observed in monolayer TMDs with excess charges (Fig. 5.12). Mak et al. [102] and Ross et al. [105] reported observation of trions in electrically gated monolayer MoS_2 and $MoSe_2$, respectively. The trion binding energies were found to be 20 and 30 meV in these studies. These values are one order of magnitude larger compared to trion binding energies in conventional quantum wells [139, 140]. For isotropic 2D semiconductors with equal electron and hole masses, the exciton binding energy is expected to be approximately 10 times larger than the trion binding energy [141, 142]. The reported exciton and trion binding energies for TMDs are roughly consistent with this rule of thumb.

A biexciton is a four-particle complex comprised of two free excitons. Biexciton emission typically occurs at a lower energy of a neutral exciton emission line and its emission intensity increases superlinearly with excitation power. Biexcitons in monolayer WSe_2 have been observed at high-power pulsed laser excitation at low temperatures [103]. Theory and experiments indicate that biexciton binding energy of 52 meV and Bohr radius of ~4 nm. Ratio of biexciton and free exciton binding energies, known as the Haynes factor, was found to be comparable with that of GaAs quantum wells [143]. Thermally activated dissociation suppresses biexciton emission peak at room temperature [103, 144].

5.2.6 *Many-Body Effects in Bilayers and van der Waals Heterostructures*

Two quantum wells separated by a thin insulating barrier layer are considered to be coupled when carriers with opposite charge in the two layers interact by Coulomb forces and form a bound state. Coupled quantum wells of InGaAs have been studied both experimentally and theoretically for Bose–Einstein condensation [154, 155] and giant Stark effects [156, 157] of such spatially indirect excitons. A bilayer TMD sheet is effectively a coupled quantum well in that electrons and holes can form a bound state across the van der Waals gap. In a typical intrinsic bilayer system, however, intralayer exciton states are anticipated to dominate. The findings by Schuller et al. [158] indicate that in-plane dipoles, i.e., intralayer excitons, are solely responsible for emission from bilayer MoS_2. Jones et al. [159] reported that in an electrostatically gated bilayer WSe_2, the trion emission peak splits into a doublet in the presence of large vertical electric fields. The authors attributed this splitting to electric-field-induced Zeeman-type splitting of energy bands associated with upper and lower layers. The doublet could then be explained by inter- and intralayer trion species. These interlayer trions consist of an intralayer exciton bound to an electron in the other layer.

Several groups have also reported observation of interlayer excitons in van der Waals heterostructures [160–162]. These interlayer excitons are effectively charge-transfer species that are commonly seen in donor-acceptor molecular complexes [163]. Monolayer group 6 TMDs typically form a type-II junction when placed in contact with each other [164, 165]. Photoemission studies indeed indicate that band alignment of a monolayer MoS_2/WSe_2 heterostack is type-II as predicted by DFT calculations [166, 167]. In such heterojunctions, excitation of intralayer excitons leads to spontaneous interlayer charge transfer and formation of interlayer excitons. Several research groups reported observation of a low-energy PL peak that does not belong to intralayer emission species and attributed it to interlayer excitons (Fig. 5.13). Rivera et al. [161] found that this low-energy emission peak redshifts with external electric field and concluded that their observation is consistent with the out-of-plane exciton dipole. Studies suggest that the brightness of interlayer excitons strongly depends on the orientation of the two layers [162]. This is consistent with the fact that misorientation of the layers renders the interlayer species indirect not only in space but also in momentum [168].

5.3 Other Layered Chalcogenides

Semiconducting nanosheets derived from other families of layered chalcogenides exhibit properties that are unique to their crystal symmetry and bonding. We briefly review chalcogenide nanosheets that have recently attracted interest for their

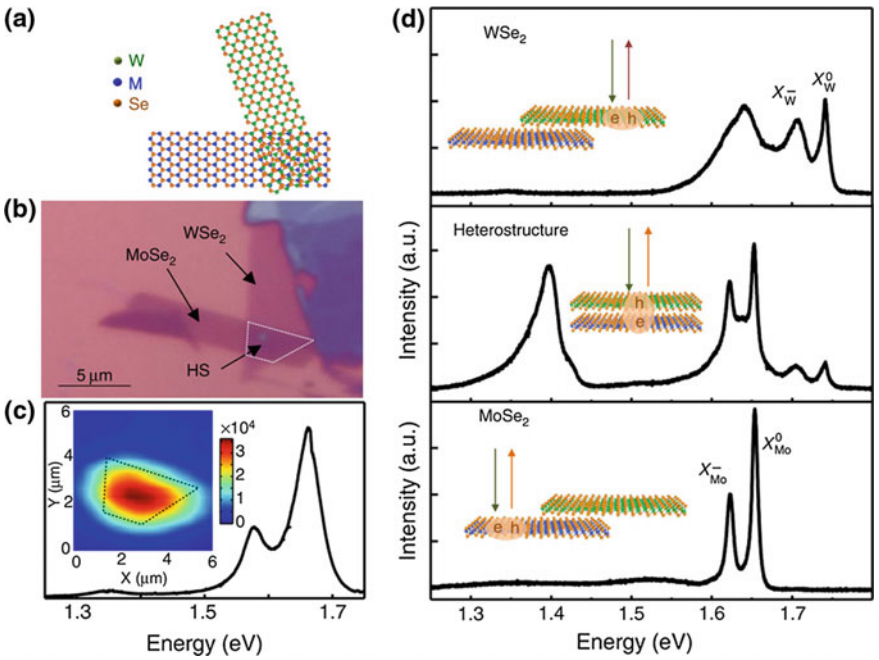

Fig. 5.13 **a** Depiction of a $MoSe_2$–WSe_2 heterostructure (HS). **b** Microscope image of a $MoSe_2$–WSe_2 HS with a *white dashed line* outlining the overlapping region. **c** Room-temperature PL of the HS. *Inset* shows spatial map of integrated PL intensity from the low-energy peak (1.273–1.400 eV), which can only be observed in HS area. **d** Photoluminescence of individual monolayers and the HS at 20 K (plotted on the same scale). Notations X_W^0 (X_W^-) and X_M^0 (X_M^-) stand for neutral (charged) exciton peak emissions due to WSe_2 and $MoSe_2$, respectively. Reprinted with permission from Ref. [161] (Copyright 2014, Nature Publishing group)

potential in nanoelectronics [169, 170], optoelectronics [171–174], solar cells [175], photonics [176], and many other fields.

5.3.1 Sn-Based Monochalcogenides

Tin monochalcogenides (SnS and SnSe) represent an interesting class of layered materials with structural in-plane anisotropy. Along with their dichalcogenide compounds SnS_2 and $SnSe_2$, they are known for their attractive thermoelectric properties. Recently reported ZT of 2.6 for SnSe at 923 K [177] its potential uses in thermoelectric devices. Bulk SnS and SnSe have orthorhombic crystal structure of distorted NaCl type. The α phase of SnS, also known as herzenbergite, is a naturally occurring mineral. Its bandgap of $\sim$1.3 eV and large absorption coefficient makes it attractive as the absorbing layer for solar cells [172, 175].

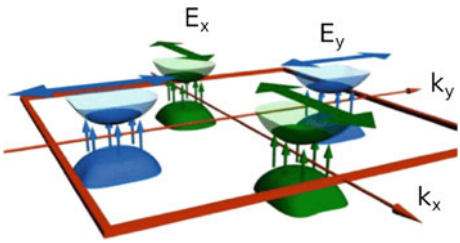

Fig. 5.14 Valley selection in monolayer SnS for an external oscillating electric field. Depending on the polarization of the field, different valleys are excited. Reprinted with permission from Ref. [171] (Copyright 2016, American Physical Society)

DFT calculations predict the bandgap of SnS to increase with decreasing thick from 1.3 eV for bulk to 1.96 eV for monolayer, similar to the case of MoS_2. The gap, however, is predicted to remain indirect for SnS for all thicknesses. In contrast, indirect-to-direct gap crossover is predicted for SnSe. Monolayer SnSe is expected to be a direct gap semiconductor with a band gap of $\sim$1.4 eV [17].

Lack of inversion symmetry in monolayer SnS and SnSe and strong spin-orbit coupling imply presence of energy degenerate but spin dependent valleys like in monolayer MoS_2. It is worth noting that according to DFT calculations, spin-orbit splitting of both valence and conductance bands reduces the electronic gap as much as 95 meV for SnS and 85 meV for SnSe [17]. Theory also predicts that the four spin- and momentum-dependent valleys in the rectangular Brillouin zone can be accessed by linearly polarized light [171] (Fig. 5.14). This is different from group 6 TMD monolayers, where a circular polarized light is needed to achieve valley polarization [99]. While experimental investigation of monolayer SnS and SnSe is limited, these attributes of SnS and SnSe make them attractive for valleytronics and spintronics.

5.3.2 Ga-Based Monochalocogenides

Monolayer GaX (X=S, Se, Te), which is made up of a X–Ga–Ga–X sandwich, has recently attracted attention for its potential as high performance photodetectors [174, 178–180]. GaTe is an exceptional member of GaX family that possesses a direct gap of $\sim$1.7 eV [181] in its bulk form. This is attributed to the unique crystal structure of monoclinic GaTe, where the Ga–Ga bonds are slightly tilted with respect to the c-axis, unlike in GaS and GaSe, whose Ga–Ga bonds are perpendicular to the layer plane [180]. Interestingly, monolayer GaTe is predicted to be an indirect gap semiconductor with a hexagonal structure [14, 182].

A recent experimental report showed that GaS and GaSe exhibit no clear signature of indirect-to-direct gap crossover as their thickness is reduced to monolayer [183]. However, the authors suggest that the difference between the direct and indirect gap in mono- and few-layer GaSe is small enough for electrons to thermally distribute over conduction band valley minima when electrons are injected into the system [183, 184]. Cathodoluminescence (CL) spectroscopy of GaSe nanosheets

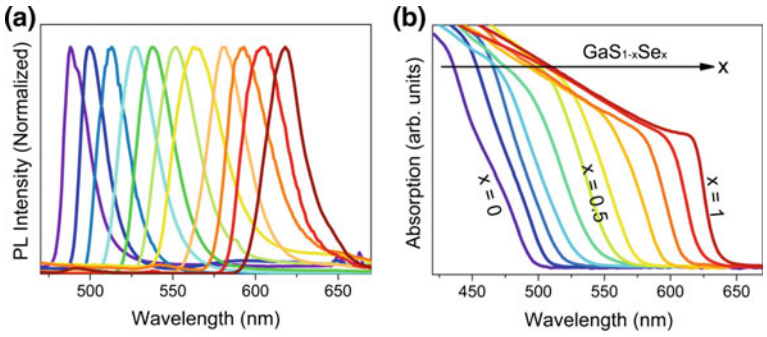

Fig. 5.15 Band gap tuning of $GaS_{1-x}Se_x$ multilayers. **a** UV-visible diffuse reflectance spectrum (in absorption) and **b** PL spectrum (at 8 K) of the $GaS_{1-x}Se_x$ nanosheets with various values of x. Reprinted with permission from Ref. [183] (Copyright 2015, American Chemical Society)

showed pronounced enhancement of the band gap emission with increasing number of layers, suggesting that the energy difference between the direct and indirect gaps are reduced for thicker flakes. Interestingly, CL spectra of GaS showed an opposite trend with emission from monolayer most strongly enhanced. Theoretical analysis [183] suggested that oxygen chemisorption induces indirect-to-direct gap transition in monolayer GaS. According to CL measurements, electronic gap of GaS (GaSe) increases from 2.5 eV (2.0 eV) to about 3.4 eV (3.3 eV) when the thickness is reduced from bulk to monolayer.

$GaS_{1-x}Se_x$ alloys are interesting for their highly tunable band gap due to the distinctly separated band gaps of GaS and GaSe. A broad tuning of PL from near-UV to red range has been demonstrated for alloys with varying sulfur and selenium compositions as shown in Fig. 5.15. The accessible range of band gaps is distinctly larger than that for group 6 TMD alloys [185–187].

5.3.3 Re-Based Dichalcogenides

ReX_2 (X=S, Se) exhibits 1T crystal structure common to TMDs but with a periodic lattice distortion and Re–Re bonding network (Fig. 5.16a, b). Owing to this structural deformation, interlayer coupling in stacked layers is weak and correspondingly, the thickness dependence of band gap is marginal. DFT predicts that ReS_2 remains a direct bandgap semiconductor independent of crystal thickness and estimates band gap of $\sim$1.35 eV for bulk and $\sim$1.43 eV for monolayer [188]. However, $ReSe_2$ is an indirect gap semiconductor with an experimentally measured optical gap of $\sim$1.26 eV and $\sim$1.32 eV for bulk and monolayer at 80 K, respectively [189]. PL intensity of RX_2 scales directly with thickness of the flakes, unlike for group 6 TMDs (Fig. 5.16c, d). A recent experimental study reported that the direct gap of bulk ReS_2 lies just 0.07 eV above the indirect gap [190].

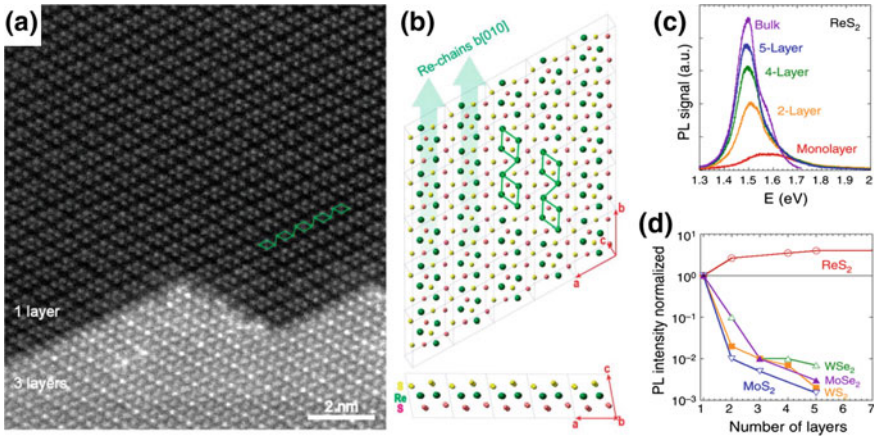

Fig. 5.16 Low magnification annular dark field (ADF) STEM image of ReS_2. The *upper part* is single-layer with the *diamond-shape-chain* phase structure, while the *lower part* is three-layer stacking. **b** Schematic illustrations of the ReS_2 atomic structure in the basal plane and cross section (Re, *green*; top S, *yellow*; bottom S, *pink*). Four Re atoms form a diamond cluster (*green line*). The *diamond-shape clusters* form a chain-like structure along the b[010] direction. **c** PL spectrum of ReS_2 flakes with different number of layers. **d** Integrated PL intensity as a function of the number of layers (normalized to that of monolayer) in ReS_2, MoS_2, $MoSe_2$, WS_2, and WSe_2. Unlike for group 6 TMDs, PL intensity of ReS_2 scales proportionally with thickness of the flake. (**a**) and (**b**) reprinted with permission from Ref. [169] (Copyright 2015, American Chemical Society), (**c**) and (**d**) reprinted with permission from Ref. [188] (Copyright 2014, American Chemical Society)

The zig-zag Re–Re bonded chains break the in-plane hexagonal symmetry and give rise to the anisotropy of optical, electrical and mechanical properties [169, 191, 192].

5.3.4 Trichalcogenides

Transition metal trichalcogenides such as TiS_3 and NbS_3 are another family of materials with strong in-plane anisotropy [170, 193]. TiS_3 has a monoclinic structure with individual layers consisting of an array of 1D chains of triangular TiS_3 units. Bulk TiS_3 is a direct gap semiconductor with an optical gap of $\sim$1 eV and a strong anisotropy in electrical conductivity [194]. Niobium trisulfide, NbS_3, is a model CDW metal that was found to exhibit characteristic 1D transport properties in thin exfoliated samples [195, 196].

Recently Island et al. [173] exfoliated 2D nanosheets of TiS_3 down to monolayer and field-effect transistors and photodetectors have been demonstrated [13, 197]. Experiments have shown that TiS_3 nanosheets exhibit pronounced in-plane anisotropy in electron transport (carrier mobility anisotropy of 2.3 and 7.6 at room temperature and 25 K, respectively) and strong linear optical dichroism,

i.e., change of absorption with rotation of polarization axis [198]. Strong quasi-1D behavior combined with large photoresponsivity [197] and predicted high carrier mobility in monolayers (10,000 $cm^2\ V^{-1}\ s^{-1}$) [170] make this material attractive for both fundamental and applied research.

5.4 Summary

The rapid development of chalcogenide nanosheet research in recent years has seen a number of key discoveries that highlight the unique potential of this class of materials in a range of novel applications. TMDs are diverse in basic material properties and rich in physics due to enhanced many-body effects and unique crystal symmetry. This chapter focused on the fundamental understanding of the electronic structure and spectroscopic signatures of excitonic effects in group 6 TMDs. There are, however, a large number of other TMDs and chalcogenides that remain unexplored in terms of their fundamental electronic properties and many-body-induced phenomena. While these 2D systems exhibit familiar features of conventional III-V quantum wells, dramatically enhanced many-body interactions, optically accessible valley quantum indices, and other emerging physical properties make them attractive for technological exploitations. Van der Waals heterostructures are not limited by lattice matching conditions, and allow preparation and study of any combination of chalcogenide nanosheets and other 2D materials. The prospects for realizing heterostructures with tailored physical properties and desired functionalities offer an exciting vista in many aspects of physical sciences and materials research.

References

1. Wilson AD, Yoffe JA (1969) The transition metal dichalcogenides discussion and interpretation of the observed optical, electrical and structural properties. Adv Phys 18:193–335
2. Murray RB, Bromley RA, Yoffe AD (1972) The band structures of some transition metal dichalcogenides. II. Group IVA; octahedral coordination. J Phys C Sol Stat Phys 5:746
3. Bromley RA, Murray RB, Yoffe AD (1972) The band structures of some transition metal dichalcogenides. III. Group VIA: trigonal prism materials. J Phys C Sol Stat Phys 5:759
4. Liang WY (1973) Optical anisotropy in layer compounds. J Phys C Solid Stat Phys 6:551–565
5. Lévy F (1979) Physics and chemistry of materials with layered structures: intercalated layered materials. Reidel, Dordrecht
6. Somoano RB, Hadek V, Rembaum A (1973) Alkali metal intercalates of molybdenum disulfide. J Chem Phys 58:697
7. Woollam JA, Somoano RB (1976) Superconducting critical fields of alkali and alkaline-earth intercalates of MoS_2. Phys Rev B 13:3843
8. Hasan MZ, Kane CL (2010) Topological insulators. Rev Mod Phys 82:3045

9. Butler SZ et al (2013) Progress, challenges, and opportunities in two-dimensional materials beyond graphene. ACS Nano 7:2898–2926
10. Kasowski RV (1973) Band structure of MoS_2 and NbS_2. Phys Rev Lett 30:1175
11. Lebègue S, Eriksson O (2009) Electronic structure of two-dimensional crystals from ab initio theory. Phys Rev B 79:115409
12. Hu KH et al (2009) Tribological properties of molybdenum disulfide nanosheets by monolayer restacking process as additive in liquid paraffin. Tribol Int 42:33–39
13. Lipatov A et al (2015) Few-layered titanium trisulfide (TiS_3) field-effect transistors. Nanoscale 7:12291–12296
14. Zolyomi V, Drummond ND, Fal'ko VI (2003) Band structure and optical transitions in atomic layers of hexagonal gallium chalcogenides. Phys Rev B 87:195403
15. Malone BD, Kaxiras E (2013) Quasiparticle band structures and interface physics of SnS and GeS. Phys Rev B 87:245312
16. Buscema M et al (2015) Photocurrent generation with two-dimensional van der Waals semiconductors. Chem Soc Rev 44:3691–3718
17. Gomes LC, Carvalho A (2015) Phosphorene analogues: isoelectronic two-dimensional group-IV monochalcogenides with orthorhombic structure. Phys Rev B 92:085406
18. Consadori F, Frindt RF (1970) Crystal size effects on the exciton absorption spectrum of WSe_2. Phys Rev B 2:4893–4896
19. Novoselov KS et al (2005) Electric field effect in atomically thin carbon films. Science 306:666
20. Chhowalla M et al (2013) The chemistry of two-dimensional layered transition metal dichalcogenide nanosheets. Nat Chem 5:263–275
21. Wang QH et al (2012) Electronics and optoelectronics of two-dimensional transition metal dichalcogenides. Nat Nanotechnol 7:699–712
22. Bhimanapati GR et al (2015) Recent advances in two-dimensional materials beyond graphene. ACS Nano 9:11509–11539
23. Gupta A, Sakthivel T, Seal S (2015) Recent development in 2D materials beyond graphene. Prog Mat Sci 73:44–126
24. Splendiani A et al (2010) Emerging photoluminescence in monolayer MoS_2. Nano Lett 10:1271–1275
25. Mak KF et al (2010) Atomically thin MoS_2: a new direct-gap semiconductor. Phys Rev Lett 105:136805
26. Zeng H et al (2012) Valley polarization in MoS_2 monolayers by optical pumping. Nat Nanotechnol 7:490–493
27. Mak KF et al (ed) (2012) Control of valley polarization in monolayer MoS_2 by optical helicity. Nat Nanotechnol 7:494–498
28. Malard AM et al (2013) Observation of intense second harmonic generation from MoS_2 atomic crystals. Phys Rev B 87:201401
29. Li Y et al (2013) Probing symmetry properties of few-layer MoS_2 and h-BN by optical second-harmonic generation. Nano Lett 13:3329–3333
30. Kumar N et al (2013) Second harmonic microscopy of monolayer MoS_2. Phys Rev B 87:161403
31. Wu W et al (2014) Piezoelectricity of single-atomic-layer MoS_2 for energy conversion and piezotronics. Nature 514:470–474
32. Zhu H et al (2015) Observation of piezoelectricity in free-standing monolayer MoS_2. Nat Nanotechnol 10:151–155
33. Zhang C et al (2014) Direct imaging of band profile in single layer MoS_2 on graphite: quasiparticle energy gap, metallic edge states and edge band bending. Nano Lett 14:2443–2447
34. Chernikov A et al (2014) Exciton binding energy and nonhydrogenic rydberg series in monolayer WS_2. Phys Rev Lett 113:076802
35. Ye Z et al (2014) Probing excitonic dark states in single-layer tungsten disulphide. Nature 513:214–218

36. Ye JT et al (2012) Superconducting dome in a gate-tuned band insulator. Science 30:1193–1196
37. Geim AK, Grigorieva IV (2013) Van der Waals heterostructures. Nature 499:419–425
38. Lee JU et al (2016) Raman signatures of polytypism in molybdenum disulfide. ACS Nano 10:1948–1953
39. Brown BE (1966) The crystal structures of WTe_2 and high-temperature $MoTe_2$. Acta Cryst 20:268–274
40. Vellinga MB, Jonge R, Haas C (1970) Semiconductor to metal transition in $MoTe_2$. J Solid Stat Chem 2:299–302
41. Coehoorn R, Haas C, de Groot RA (1987) Electronic structure of $MoSe_2$, MoS_2, and WSe_2. II. The nature of the optical band gaps. Phys Rev B 35:6203–6206
42. Novoselov KS et al (2005) Two-dimensional atomic crystals. PNAS 102:10451
43. Schafer H (1964) Chemical transport reactions. Academic Press, New York
44. Koma A, Sunouchi K, Miyajima T (1984) Fabrication and characterization of heterostructures with subnanometer thickness. Microelectron Eng 2:129–136
45. Zheng J et al (2014) High yield exfoliation of two-dimensional chalcogenides using sodium naphthalenide. Nature Commun 5:2995
46. Nicolosi V et al (2013) Liquid exfoliation of layered materials. Science 340:6139
47. Amara KK et al (2014) Wet chemical thinning of molybdenum disulfide down to its monolayer. APL Mater 2:092509
48. Huang Y et al (2013) An innovative way of etching MoS_2: characterization and mechanistic investigation. Nano Res 6:200
49. Liu Y et al (2013) Layer-by-layer thinning of MoS_2 by plasma. ACS Nano 7:4202
50. Castellanos-Gomez A et al (2012) Laser-thinning of MoS_2: on demand generation of a single-layer semiconductor. Nano Lett 12:3187
51. Altavilla C, Sarno M, Ciambelli P (2011) A novel wet chemistry approach for the synthesis of hybrid 2D free-floating single or multilayer nanosheets of MS_2@oleylamine (M=Mo, W). Chem Mater 23:3879
52. Tan LK et al (2014) Atomic layer deposition of a MoS_2 film. Nanoscale 6:10584
53. Zhan Y et al (2012) Large-area vapor-phase growth and characterization of MoS_2 atomic layers on a SiO_2 substrate. Small 8:966
54. Liu K-K et al (2012) Growth of large-area and highly crystalline MoS_2 thin layers on insulating substrates. Nano Lett 12:1538
55. Lee Y-H et al (2012) Synthesis of large-area MoS_2 atomic layers with chemical vapor deposition. Adv Mater 24:2320
56. Amani M et al (2013) Electrical performance of monolayer MoS_2 field-effect transistors prepared by chemical vapor deposition. Appl Phys Lett 102:193107
57. van der Zande AM et al (2013) Grains and grain boundaries in highly crystalline monolayer molybdenum disulphide. Nat Mater 12:554
58. Wang H et al (2012) Integrated circuits based on bilayer MoS_2 transistors. Nano Lett 12:4674
59. Najmaei S et al (2013) Vapour phase growth and grain boundary structure of molybdenum disulphide atomic layers. Nat Mater 12:754
60. Yu Y et al (2013) Controlled scalable synthesis of uniform, high-quality monolayer and few-layer MoS_2 films. Sci Rep 3:1866
61. Gong C et al (2013) Metal contacts on physical vapor deposited monolayer MoS_2. ACS Nano 7:11350
62. Liu Y et al (2014) Mesoscale imperfections in MoS_2 atomic layers grown by a vapor transport technique. Nano Lett 14:4682
63. Liu H et al (2013) Statistical study of deep submicron dual-gated field-effect transistors on monolayer chemical vapor deposition molybdenum disulfide films. Nano Lett 13:2640
64. Liu B et al (2014) High-performance chemical sensing using schottky-contacted chemical vapor deposition grown monolayer MoS_2 transistors. ACS Nano 8:5304

65. Najmaei S et al (2014) Electrical transport properties of polycrystalline monolayer molybdenum disulfide. ACS Nano 8:7930
66. Schmidt H et al (2014) Transport properties of monolayer MoS_2 grown by chemical vapor deposition. Nano Lett 14:1909
67. Dumcenco D et al (2015) Large-area epitaxial monolayer MoS_2. ACS Nano 9:4611–4620
68. Zhu W et al (2014) Electronic transport and device prospects of monolayer molybdenum disulphide grown by chemical vapour deposition. Nat Commun 5:3087
69. Wang X et al (2014) Chemical vapor deposition growth of crystalline monolayer $MoSe_2$. ACS Nano 8:5125
70. Shaw JC et al (2014) Chemical vapor deposition growth of monolayer $MoSe_2$ and nanosheets. Nano Res 7:1
71. Zhang Y et al (2013) Controlled growth of high-quality monolayer WS_2 layers on sapphire and imaging its grain boundary. ACS Nano 7:8963
72. Sirlina T et al (2000) Study on preparation, growth mechanism, and optoelectronic properties of highly oriented WSe_2 thin films. J Mater Res 15:2636
73. Huang J-K et al (2014) Large-area synthesis of highly crystalline WSe_2 monolayers and device applications. ACS Nano 8:923
74. Gong Y et al (2014) Band gap engineering and layer-by-layer mapping of selenium-doped molybdenum disulfide. Nano Lett 14:442
75. Lin Y-C et al (2014) Properties of individual dopant atoms in single-layer MoS_2: atomic structure, migration, and enhanced reactivity. Adv Mater 26:2857
76. Hong J et al (2015) Exploring atomic defects in molybdenum disulphide monolayers. Nat Commun 6:6293
77. Zhou W et al (2013) Intrinsic structural defects in monolayer molybdenum disulfide. Nano Lett 13:2615
78. Lu C-P et al (2014) Bandgap, mid-gap states, and gating effects in MoS_2. Nano Lett 14:4628
79. Tongay S et al (2013) Defects activated photoluminescence in two-dimensional semiconductors: interplay between bound, charged, and free excitons. Sci Rep 3:2657
80. Radisavljevic B et al (2011) Single-layer MoS_2 transistors. Nat Nanotechnol 6:147
81. Kim S et al (2012) High-mobility and low-power thin-film transistors based on multilayer MoS_2 crystals. Nat Commun 3:1011
82. Baugher BWH et al (2013) Intrinsic electronic transport properties of high-quality monolayer and bilayer MoS_2. Nano Lett 13:4212
83. Wang Z et al (2013) Hopping transport through defect-induced localized states in molybdenum disulphide. Nat Commun 4:2642
84. Yu Z et al (2014) Towards intrinsic charge transport in monolayer molybdenum disulfide by defect and interface engineering. Nat Commun 5:5290
85. Liu G-B et al (2015) Electronic structures and theoretical modelling of two-dimensional group-VIB transition metal dichalcogenides. Chem Soc Rev 44:2643–2663
86. Zhao W et al (2013) Evolution of electronic structure in atomically thin sheets of WS_2 and WSe_2. ACS Nano 7:791–797
87. Tongay S et al (2012) Thermally driven crossover from indirect toward direct bandgap in 2D semiconductors: $MoSe_2$ versus MoS_2. Nano Lett 12:5576–5580
88. Zhang Y et al (2014) Direct observation of the transition from indirect to direct bandgap in atomically thin epitaxial $MoSe_2$. Nat Nanotechnol 9:111–115
89. Jin W et al (2013) Direct measurement of the thickness-dependent electronic band structure of MoS_2 using angle-resolved photoemission spectroscopy. Phys Rev Lett 111:106801
90. Zeng H et al (2013) Optical signature of symmetry variations and spin-valley coupling in atomically thin tungsten dichalcogenides. Sci Rep 3:1608
91. Zhang C et al (2015) Probing critical point energies of transition metal dichalcogenides: surprising indirect gap of single layer WSe_2. Nano Lett 15:6494–6500
92. Lezama IG et al (2015) Indirect-to-direct band gap crossover in few-layer $MoTe_2$. Nano Lett 15:2336–2342

93. Schmidt H, Giustiniano F, Eda G (2015) Electronic transport properties of transition metal dichalcogenide field-effect devices: surface and interface effects. Chem Soc Rev 44:7715–7736
94. Zhao W, Mendes Ribeiro R, Eda G (2015) Electronic structure and optical signatures of semiconducting transition metal dichalcogenide nanosheets. Acc Chem Res 48:91–99
95. Yoffe AD (2002) Low-dimensional systems: quantum size effects and electronic properties of semiconductor microcrystallites (zero-dimensional systems) and some quasi-two-dimensional systems. Adv Phys 51:799–890
96. Cheiwchanchamnangij T, Lambrecht WRL (2012) Quasiparticle band structure calculation of monolayer, bilayer, and bulk MoS_2. Phys Rev B 85:205302
97. Tongay S et al (2013) Broad-range modulation of light emission in two-dimensional semiconductors by molecular physisorption gating. Nano Lett 13:2831–2836
98. Komsa HP, Krasheninnikov AV (2012) Effects of confinement and environment on the electronic structure and exciton binding energy of MoS_2 from first principles. Phys Rev B 86:241201
99. Yu H et al (2015) Valley excitons in two-dimensional semiconductors. Natl Sci Rev 2:57–70
100. Xu X et al (2014) Spin and pseudospins in layered transition metal dichalcogenides. Nat Phys 10:343–350
101. Zhao W et al (2013) Origin of indirect optical transitions in few-layer MoS_2, WS_2, and WSe_2. Nano Lett 13:5627–5634
102. Mak KF et al (2013) Tightly bound trions in monolayer MoS_2. Nat Mater 12:207–211
103. You Y et al (2015) Observation of biexcitons in monolayer WSe_2. Nat Phys 11:477–481
104. Jones AM et al (2013) Optical generation of excitonic valley coherence in monolayer WSe_2. Nat Nanotechnol 8:634–638
105. Ross JS et al (2013) Electrical control of neutral and charged excitons in a monolayer semiconductor. Nat Commun 4:1474
106. Castellanos-Gomez A et al (2013) Local strain engineering in atomically thin MoS_2. Nano Lett 13:5361
107. Conley HJ et al (2013) Bandgap engineering of strained monolayer and bilayer MoS_2. Nano Lett 13:3626
108. Qiu DY, da Jornada FH, Louie SG (2013) Optical spectrum of MoS_2: many-body effects and diversity of exciton states. Phys Rev Lett 111:216805
109. Beal AR, Hughes HP (1979) Kramers-Kronig analysis of the reflectivity spectra of 2H-MoS_2, 2H-$MoSe_2$ and 2H-$MoTe_2$. J Phys C Solid Stat Phys 12:881
110. Carvalho A, Ribeiro RM, Castro Neto AH (2013) Band nesting and the optical response of two-dimensional semiconducting transition metal dichalcogenides. Phys Rev B 88:115205
111. Kumar R, Verzhbitskiy I, Eda G (2015) Strong optical absorption and photocarrier relaxation in two-dimensional semiconductors. IEEE J Quant Elec 51:0600206
112. Britnell L et al (2013) Strong light-matter interactions in heterostructures of atomically thin films. Science 340:1311–1314
113. Feng J et al (2012) Strain-engineered artificial atom as a broad-spectrum solar energy funnel. Nat Photon 6:865–871
114. Nair RR et al (2008) Fine structure constant defines visual transparency of graphene. Science 320:1308
115. Yun WS et al (2012) Thickness and strain effects on electronic structures of transition metal dichalcogenides: 2H-MX_2 semiconductors (M=Mo, W; X=S, Se, Te). Phys Rev B 85:033305
116. Kuc A, Zibouche N, Heine T (2011) Influence of quantum confinement on the electronic structure of the transition metal sulfide TS_2. Phys Rev B 83:245213
117. Ramasubramaniam A, Naveh D, Towe E (2011) Tunable band gaps in bilayer transition-metal dichalcogenides. Phys Rev B 84:205325
118. Klein A et al (2001) Electronic band structure of single-crystal and single-layer WS_2: influence of interlayer van der Waals interactions. Phys Rev B 64:205416

119. Ugeda MM et al (2014) Giant bandgap renormalization and excitonic effects in a monolayer transition metal dichalcogenide semiconductor. Nat Mater 13:1091–1095
120. Chernikov A et al (2015) Electrical tuning of exciton binding energies in monolayer WS_2. Phys Rev Lett 115:126802
121. Yuan H et al (2013) Zeeman-type spin splitting controlled by an electric field. Nat Phys 9:563–569
122. Ruppert C, Aslan OB, Heinz TF (2014) Optical properties and band gap of single- and few-layer $MoTe_2$ crystals. Nano Lett 14:6231–6236
123. Py MA, Haering RR (1983) Structural destabilization induced by lithium intercalation in MoS_2 and related compounds. Can J Phys 61:76–84
124. Voiry D, Mohite A, Chhowalla M (2015) Phase engineering of transition metal dichalcogenides. Chem Soc Rev 44:2702–2712
125. Eda G et al (2011) Photoluminescence from chemically exfoliated MoS_2. Nano Lett 11:5111–5116
126. Joensen P, Frindt RF, Morrison SR (1986) Single-layer MoS_2. Mater Res Bull 21:457–461
127. Papageorgopoulos CA, Jaegermann W (1995) Li intercalation across and along the van der Waals surfaces of MoS_2 (0001). Surf Sci 338:83–93
128. Li LJ et al (2016) Controlling many-body states by the electric-field effect in a two-dimensional material. Nature 529:185–189
129. Zhang C et al (2014) Absorption of light by excitons and trions in monolayers of metal dichalcogenide MoS_2: experiments and theory. Phys Rev B 89:205436
130. Nguyen DT et al (2011) Elastic exciton-exciton scattering in photoexcited carbon nanotubes. Phys Rev Lett 107:127401
131. Qiu DY, da Jornada FH, Louie SG (2015) Erratum: optical spectrum of MoS_2: many-body effects and diversity of exciton states. Phys Rev Lett 115:119901
132. Miller RC et al (1981) Observation of the excited level of excitons in GaAs quantum wells. Phys Rev B 24:1134
133. Greene RL, Bajaj KK, Phelps DE (1984) Energy levels of Wannier excitons in GaAs−$Ga_{1-x}Al_xAs$ quantum-well structures. Phys Rev B 29:1807
134. Beal AR, Knights JC, Liang WY (1972) Transmission spectra of some transition metal dichalcogenides. II. Group VIA: trigonal prismatic coordination. Phys C Sol Stat Phys 5:3540–3551
135. Klots AR et al (2014) Probing excitonic states in suspended two-dimensional semiconductors by photocurrent spectroscopy. Sci Rep 4:6608
136. Hill HM et al (2015) Observation of excitonic rydberg states in monolayer MoS_2 and WS_2 by photoluminescence excitation spectroscopy. Nano Lett 13:2992–2997
137. Zhu B, Chen X, Cui X (2015) Exciton binding energy of monolayer WS_2. Sci Rep 5:9218
138. Berkelbach TC, Hybertsen MS, Reichman DR (2013) Theory of neutral and charged excitons in monolayer transition metal dichalcogenides. Phys Rev B 88:045318
139. Kheng K et al (1993) Observation of negatively charged excitons X^- in semiconductor quantum wells. Phys Rev Lett 71:1752
140. Finkelstein G, Shtrikman H, Bar-Joseph I (1995) Optical spectroscopy of a two-dimensional electron gas near the metal-insulator transition. Phys Rev Lett 74:976
141. Sergeev RA, Suris RA (2001) Ground-state energy of X^- and X^+ trions in a two-dimensional quantum well at an arbitrary mass ratio. Phys Sol Stat 43:746–751
142. Thilagam A (1997) Two-dimensional charged-exciton complexes. Phys Rev B 55:7804–7808
143. Klingshirn CF (2007) Semiconductor Optics. Springer, Berlin
144. He Z et al (2016) Biexciton formation in bilayer tungsten disulfide. ACS Nano 10:2176–2183
145. Mai C et al (2014) Many-body effects in valleytronics: direct measurement of valley lifetimes in single-layer MoS_2. Nano Lett 14:202–206
146. Sie EJ et al (2015) Intervalley biexcitons and many-body effects in monolayer MoS_2. Phys Rev B 92:125417

147. Mitioglu AA et al (2013) Optical manipulation of the exciton charge state in single-layer tungsten disulfide. Phys Rev B 88:245403
148. Plechinger G et al (2015) Identification of excitons, trions and biexcitons in single-layer WS_2. Phys Stat Sol RRL 9:457–467
149. Shang J et al (2015) Observation of excitonic fine structure in a 2D transition-metal dichalcogenide semiconductor. ACS Nano 9:647–655
150. Liu H et al (2014) Dense network of one-dimensional midgap metallic modes in monolayer $MoSe_2$ and their spatial undulations. Phys Rev Lett 113:066105
151. He K et al (2014) Tightly bound excitons in monolayer WSe_2. Phys Rev Lett 113:026803
152. Wang G et al (2015) Giant enhancement of the optical second-harmonic emission of WSe_2 monolayers by laser excitation at exciton resonances. Phys Rev Lett 114:097403
153. Yang J et al (2015) Robust excitons and trions in monolayer $MoTe_2$. ACS Nano 9:6603–6609
154. Zhu X et al (1995) Exciton condensate in semiconductor quantum well structures. Phys Rev Lett 74:1633
155. Butov LV et al (2002) Towards Bose-Einstein condensation of excitons in potential traps. Nature 417:47–52
156. Fox AM et al (1992) Suppression of the observation of Stark ladders in optical measurements on superlattices by excitonic effects. Phys Rev B 46:15365
157. Kato Y et al (1994) Observation of the Stark effect in coupled quantum wells by electroluminescence and circularly polarized photoluminescence excitation spectroscopy. J Appl Phys 75:7476
158. Schuller JA et al (2013) Orientation of luminescent excitons in layered nanomaterials. Nat Nanotechnol 8:271–276
159. Jones AM et al (2014) Spin–layer locking effects in optical orientation of exciton spin in bilayer WSe_2. Nat Phys 10:130–134
160. Fang H et al (2014) Strong interlayer coupling in van der Waals heterostructures built from single-layer chalcogenides. PNAS 111:6198–6202
161. Rivera P et al (2015) Observation of long-lived interlayer excitons in monolayer $MoSe_2$–WSe_2 heterostructures. Nat Commun 6:6242
162. Rivera P et al (2016) Valley-polarized exciton dynamics in a 2D semiconductor heterostructure. Science 351:688–691
163. Li G, Zhu R, Yang Y (2012) Polymer solar cells. Nat Photonics 6:153–161
164. Kośmider K, Fernández-Rossier J (2013) Electronic properties of the MoS_2–WS_2 heterojunction. Phys Rev B 87:075451
165. Özçelik VO et al (2016) Band alignment of 2D semiconductors for designing heterostructures with momentum space matching. Phys Rev B 94:035125
166. Kang J et al (2013) Band offsets and heterostructures of two-dimensional semiconductors. Appl Phys Lett 102:012111
167. Terrones H, Lopez-Urias F, Terrones M (2013) Novel hetero-layered materials with tunable direct band gaps by sandwiching different metal disulfides and diselenides. Sci Rep 3:1549
168. Yu H et al (2015) Anomalous light cones and valley optical selection rules of interlayer excitons in twisted heterobilayers. Phys Rev Lett 115:187002
169. Lin Y-C et al (2015) Single-layer ReS_2: two-dimensional semiconductor with tunable in-plane anisotropy. ACS Nano 9:11249–11257
170. Dai J, Zeng XC (2015) Titanium trisulfide monolayer: theoretical prediction of a new direct-gap semiconductor with high and anisotropic carrier mobility. Angew Chem Int Ed 54:7572–7576
171. Rodin AS et al (2016) Valley physics in tin (II) sulfide. Phys Rev B 93:045431
172. Tritsaris GA, Malone BD, Kaxiras E (2013) Optoelectronic properties of single-layer, double-layer, and bulk tin sulfide: a theoretical study. J Appl Phys 113:233507
173. Island JO et al (2015) TiS_3 transistors with tailored morphology and electrical properties. Adv Mater 27:2595–2601
174. Hu P et al (2012) Synthesis of few-layer GaSe nanosheets for high performance photodetectors. ACS Nano 6:5988–5994

175. Ramakrishna Reddy KT, Koteswara Reddy N, Miles RW (2006) Photovoltaic properties of SnS based solar cells. Sol Energy Mater Sol Cells 90:3041–3046
176. Schwarz S et al (2014) Two-dimensional metal−chalcogenide films in tunable optical microcavities. Nano Lett 14:7003–7008
177. Zhao L-D et al (2014) Ultralow thermal conductivity and high thermoelectric figure of merit in SnSe crystals. Nature 508:373–377
178. Li X et al (2014) Controlled vapor phase growth of single crystalline, two-dimensional GaSe crystals with high photoresponse. Sci Rep 4:5497
179. Hu P et al (2013) Highly responsive ultrathin GaS nanosheet photodetectors on rigid and flexible substrates. Nano Lett 13:1649–1654
180. Liu F et al (2014) High-sensitivity photodetectors based on multilayer GaTe flakes. ACS Nano 8:752–760
181. Sanchez-Royo JF et al (2002) Angle-resolved photoemission study and first-principles calculation of the electronic structure of GaTe. Phys Rev B 65:115201
182. Zhang HL, Hennig RG (2003) Single-layer group-III monochalcogenide photocatalysts for water splitting. Chem Mater 25:3232–3238
183. Jung CS et al (2015) Red-to-ultraviolet emission tuning of two-dimensional gallium sulfide/selenide. ACS Nano 9:9585–9593
184. Ma Y et al (2013) Tunable electronic and dielectric behavior of GaS and GaSe monolayers. Phys Chem Chem Phys 15:7098–7105
185. Li H et al (2014) Growth of alloy $MoS_{2x}Se_{2(1-x)}$ nanosheets with fully tunable chemical compositions and optical properties. J Am Chem Soc 136:3756–3759
186. Dumcenco DO et al (2013) Visualization and quantification of transition metal atomic mixing in $Mo_{1-x}W_xS_2$ single layers. Nat Commun 4:1351
187. Zhang M et al (2014) Two-dimensional molybdenum tungsten diselenide alloys: photoluminescence, raman scattering, and electrical transport. ACS Nano 8:7130–7137
188. Tongay S et al (2014) Monolayer behaviour in bulk ReS_2 due to electronic and vibrational decoupling. Nat Commun 5:3252
189. Zhao H et al (2015) Interlayer interactions in anisotropic atomically thin rhenium diselenide. Nano Res 8:3651–3661
190. Aslan OB et al (2016) Linearly polarized excitons in single- and few-layer ReS_2 crystals. ACS Photon 3:96–101
191. Chenet DA et al (2015) In-plane anisotropy in mono- and few-layer ReS_2 probed by Raman spectroscopy and scanning transmission electron microscopy. Nano Lett 15:5667–5672
192. Zhong H-X et al (2015) Quasiparticle band gaps, excitonic effects, and anisotropic optical properties of the monolayer distorted 1T diamond-chain structures ReS_2 and $ReSe_2$. Phys Rev B 92:115438
193. Jin Y, Li X, Yang J (2015) Single layer of MX_3 (M=Ti, Zr; X=S, Se, Te): a new platform for nano-electronics and optics. Phys Chem Chem Phys 17:18665–18669
194. Gorlova I et al (2012) Nonlinear conductivity of quasi-one-dimensional layered compound TiS_3. Physica B 407:1707
195. Zaitsev-Zotov SV, Pokrovskii V Ya, Monceau P (2001) Transition to 1D conduction with decreasing thickness of the crystals of TaS_3 and $NbSe_3$ quasi-1D conductors. J Exp Theor Phys Lett 73:25–27
196. Slot E et al (2004) One-dimensional conduction in charge-density-wave nanowires. Phys Rev Lett 93:176602
197. Island JO et al (2014) Ultrahigh photoresponse of few-layer TiS_3 nanoribbon transistors. Adv Opt Mat 2:641–645
198. Island JO et al (2016) Titanium trisulfide (TiS_3): a 2D semiconductor with quasi-1D optical and electronic properties. Sci Rep 6:22214